JOURNAL OF PROPULSION AND POWER
Vol. 25, No. 2, March–April 2009

Aluminum Combustion Driven Instabilities in Solid Rocket Motors

Stany Gallier* and Franck Godfroy†
SNPE Matériaux Energétiques, 91710 Vert le Petit, France

DOI: 10.2514/1.37664

This work describes an unreported instability found out by numerical simulations on a solid rocket motor. A simple motor with a cylindrical port is considered and predicted to be stable by single-phase computational fluid dynamics computations. When aluminum combustion is modeled, the motor experiences a strong instability on the first longitudinal acoustic mode. However, no vortex shedding is observed, meaning that it is a genuine combustion instability. A detailed numerical study leads to the conclusion that the instability is thermoacoustic and results from a coupling between chamber acoustics and aluminum combustion heat release. A parametric study points out the importance of aluminum distributed combustion, particularly the thickness of the combustion zone and the aluminum heat of reaction. Theoretical assessment of this instability is also obtained by revisiting the acoustic balance theory. An additional thermoacoustic stability integral is derived and appears to be a driving term. This term also helps to shed light on this instability and explains some of the computational fluid dynamics results. In particular, the underlying mechanism is found to be primarily caused by the acoustic boundary layer which creates high acoustic velocities that enhance heat release from burning aluminum particles.

Nomenclature

a	=	sound velocity
B	=	Spalding number [Eq. (5)]
C_d	=	drag coefficient
C_P	=	specific heat at constant pressure
D	=	particle diameter
E	=	total energy
e_{comb}	=	thickness of aluminum combustion zone
$\mathbf{e}_x$	=	axial direction unit vector
F	=	acoustic boundary-layer term [Eq. (B6)]
$\mathbf{F}_d$	=	drag force vector
f	=	frequency
H	=	transfer function [Eq. (A9)]
i	=	$\sqrt{-1}$
k	=	wave number ($=\pi/L$)
L	=	motor length
L_v	=	latent heat of vaporization
Le	=	Lewis number
m	=	propellant mass rate
N_p	=	number of particles per unit volume
Nu	=	Nusselt number
Pr	=	Prandtl number
p	=	pressure
Q	=	heat of reaction per unit mass
Q_v	=	convective heat transfer
q	=	heat release rate
R	=	port radius
Re	=	Reynolds number
r	=	radial position ($r = 0$ at centerline)
S	=	Strouhal number ($=\omega R/v_{\text{inj}}$)
$\mathbf{S}$	=	source term vector
St	=	Stokes number ($=\omega\tau_d$)
T	=	temperature or period
t_c	=	droplet combustion time
$\mathbf{U}$	=	velocity vector
(u, v)	=	axial and radial velocities
$\mathbf{W}$	=	conservative variable vector
x	=	axial position
α	=	growth rate
α_p	=	particle volume fraction
α_{PC}	=	particle combustion growth rate [Eq. (12)]
γ	=	specific heat ratio
$\delta\mathbf{U}$	=	relative velocity vector ($=\mathbf{U}_p - \mathbf{U}_g$)
ε	=	nondimensional distance to surface ($=1 - r/R$)
$\varepsilon_{\text{comb}}$	=	nondimensional thickness ($=e_{\text{comb}}/R$)
η	=	amplitude of pressure perturbation
κ	=	particle mass loading ($=\rho_p\alpha_p/\rho_g$)
λ	=	gas thermal conductivity
μ	=	dynamic viscosity
ξ	=	viscous parameter [Eq. (B3)]
ρ	=	density
τ_d	=	particle dynamic relaxation time
$\tau_{d,s}$	=	Stokes particle dynamic relaxation time ($=\rho_p D^2/18\mu$)
τ_t	=	particle thermal relaxation time ($=3/2\, Pr\, C_{P,p}/C_{P,g}\tau_d$)
ψ	=	pressure spatial mode shape
ω	=	pulsation ($=2\pi f$)
$\dot{\omega}$	=	mass release rate for aluminum combustion

Subscripts

comb	=	combustion
g	=	gas phase
inj	=	injection conditions (=at propellant surface)
p	=	particle phase
res	=	oxide residue (=alumina)
sat	=	saturation conditions
t	=	nozzle throat conditions

Received 21 March 2008; revision received 18 December 2008; accepted for publication 18 December 2008. Copyright © 2009 by SNPE Matériaux Energétiques. Published by the American Institute of Aeronautics and Astronautics, Inc., with permission. Copies of this paper may be made for personal or internal use, on condition that the copier pay the $10.00 per-copy fee to the Copyright Clearance Center, Inc., 222 Rosewood Drive, Danvers, MA 01923; include the code 0748-4658/09 $10.00 in correspondence with the CCC.

*Research Engineer, Department of Aerodynamics and Combustion; s.gallier@snpe.com.

†Research Engineer, Department of Aerodynamics and Combustion; f.godfroy@snpe.com.

I. Introduction

A NUMBER of large solid rocket motors, including Ariane 5 [1], the space shuttle [2], or the Titan family [3,4], are reported to exhibit instabilities during operation. Those instabilities become apparent as thrust oscillations that involve vibrations detrimental to carrying a load. Following Culick [5], the chief mechanisms for combustion instabilities in solid rockets are the propellant

combustion (pressure coupling and velocity coupling) and the hydrodynamic instabilities (vortex sheddings). For large motors, however, active research during the past years showed that instabilities are generally dominated by a coupling between chamber acoustics (mostly axial modes) and hydrodynamic instability. The latter arises from vortex shedding stemming either from unstable shear layers (caused by an obstacle, such as a protruding inhibitor [3,4,6,7], or by specific grain shapes [8]), or surface instability [9]. This instability, so-called surface vortex shedding or parietal vortex shedding (PVS), has been supported by experimental [10,11], numerical [9,12], or analytical theories [13,14], and has occurred to be a powerful source of instability in large solid rockets.

Although aluminum combustion is widely studied, its eventual participation to instability in solid rockets using aluminized propellants has not been considered so far. Actually, little notice has been taken of its potential role on motor stability probably because generally instabilities can be satisfactorily explained by other mechanisms, especially propellant combustion and vortex shedding. However, Culick [5] proposed that distributed combustion of aluminum could possibly play a role on stability, but he states that there is no unambiguous evidence that combustion within the volume contributes significantly as a cause of combustion instabilities. Similarly, Kuentzmann [15] stressed that distributed combustion is known to drive instabilities in liquid rockets [16] and this could also stand for aluminum in solid rockets. Indeed, recent work from Dupays and Vuillot [17,18] theoretically proved that mass release from a cloud of vaporizing droplets could drive acoustic waves.

As far as the authors know, the only extensive works on that issue remain the ones from Raun and Beckstead [19] and Brooks and Beckstead [20]. They studied the effect of aluminum distributed combustion in a Rijke burner and proved that aluminum combustion can drive instability, based on both experimental and theoretical grounds. Yet, they concluded that amplification is mainly due to the change in gas axial temperature profile which causes the location of the velocity antinodes to shift relative to the Rijke burner flame and thereby induce an increase in the flame response. This conclusion can clearly not be extrapolated to solid rocket motors because gas axial temperature is rather constant in the chamber and propellant flame is virtually a surface process. Therefore, the problem of instability driven by aluminum combustion is still open in solid rocket motors and even at the present time, Culick [5] states that no calculations exist assessing quantitatively the possible contribution of particle combustion to linear stability of solid rocket motors.

This view is on the way to being reconsidered, at least numerically. The maturity of computational fluid dynamics (CFD) and models for solid propulsion makes it possible for a detailed numerical description of motor internal aerodynamics. The present work intends to demonstrate that aluminum combustion does indeed drive instability, by considering two-phase flow numerical simulations on a test motor configuration. Some theoretical grounds, using classical linear stability, also favor a destabilizing contribution of aluminum distributed combustion on solid rocket motor stability.

II. Numerical Modeling

A. Governing Equations

Compressible Navier–Stokes equations are solved with perfect gas law. As for two-phase flow, a two-way coupling Eulerian model is used. The particle phase is supposed dilute (volume fraction $\alpha_p \ll 1$), monodisperse (i.e., a single class of injected particles), and assumed to be spherical. The equation reads

$$\frac{\partial}{\partial t}\begin{pmatrix}\mathbf{W}_g\\ \mathbf{W}_p\end{pmatrix} + \nabla.\begin{pmatrix}\mathbf{F}_g\\ \mathbf{F}_p\end{pmatrix} = \begin{pmatrix}\mathbf{S}_g\\ \mathbf{S}_p\end{pmatrix} \tag{1}$$

$\mathbf{W}$ denotes the conservative variable vector, $\mathbf{F}$ the flux vector, and $\mathbf{S}$ the source term vector. Subscript g (respectively, p) stands for the gas phase (respectively, particle phase). Expressions for $\mathbf{W}_g$ and $\mathbf{F}_g$ are classical compressible Navier–Stokes equations for the gas phase and are not recalled here. Conservation imposes that $\mathbf{S}_g = -\mathbf{S}_p$.

For particles, the equations read as

$$\mathbf{W}_p = \begin{pmatrix}\rho_p\alpha_p\\ \rho_p\alpha_p\mathbf{U}_p\\ \rho_p\alpha_p E_p\\ N_p\end{pmatrix} \qquad \mathbf{F}_p = \begin{pmatrix}\rho_p\alpha_p\mathbf{U}_p\\ \rho_p\alpha_p\mathbf{U}_p\otimes\mathbf{U}_p\\ \rho_p\alpha_p\mathbf{U}_p E_p\\ \mathbf{U}_p N_p\end{pmatrix}$$
$$\mathbf{S}_p = -\begin{pmatrix}\dot\omega\\ \dot\omega\mathbf{U}_p - \mathbf{F}_d\\ \dot\omega E_p - \mathbf{F}_d.\mathbf{U}_p + \dot\omega(L_v+Q) - Q_v\\ 0\end{pmatrix} \tag{2}$$

where ρ_p is the particle material density (assumed constant), α_p the particle volume fraction, $\mathbf{U}_p$ the particle velocity vector, E_p the particle total energy, and N_p the number of particles per unit volume. Note that the equation on N_p is a simple transport equation as neither coalescence nor breakup is considered.

The particle diameter D is not explicitly tracked and is computed via

$$D = \left(\frac{6\alpha_p}{\pi N_p}\right)^{1/3} \tag{3}$$

Aluminum combustion is supposed to follow a classical D^2 law so that the expression for its mass release rate $\dot\omega$ is, under unit Lewis assumption:

$$\dot\omega = 2\pi\frac{\mu}{Pr}N_p D\,\ell_n(1+B)\,[1+0.3\,Re_p^{1/2}\,Pr^{1/3}] \tag{4}$$

with μ the dynamic viscosity, Pr the Prandtl number, and B the Spalding number given by

$$B = \frac{C_{P,g}(T_g - T_p) + Q}{L_v} \tag{5}$$

with $C_{P,g}$ the gas specific heat, T the temperature, Q the heat of reaction (per unit mass), and L_v the latent heat of vaporization. This simple model assumes that the gas released is identical to the surrounding gas. Moreover, it is supposed that aluminum combustion takes place through individual droplets and is not affected by group combustion.

The bracketed term in Eq. (4) is the classical Ranz–Marshall correlation [21] that accounts for convective effects on mass rate. In that expression, the Reynolds number Re_p is based on particle diameter and relative velocity:

$$Re_p = \frac{\rho_g\|\delta\mathbf{U}\|D}{\mu} \quad \text{with} \quad \delta\mathbf{U} \equiv \mathbf{U}_p - \mathbf{U}_g \tag{6}$$

However, as soon as the particle diameter has decreased until a user-prescribed diameter D_{res}, the combustion is stopped ($\dot\omega = 0$) and the particle is now supposed nonreacting: its diameter will remain at $D = D_{\text{res}}$. The purpose is to account for the physical existence of a nonvanishing inert alumina (Al_2O_3) residue.

The drag force vector $\mathbf{F}_d$, with the Clift correlation [22] for the drag coefficient C_d, reads

$$\mathbf{F}_d = -\frac{1}{8}\pi D^2 N_p\frac{C_d}{1+B}\rho_g\|\delta\mathbf{U}\|\cdot\delta\mathbf{U}$$
$$C_d = \max\left(0.44, \frac{24(1+0.15\,Re_p^{0.687})}{Re_p}\right) \tag{7}$$

As for heat transfer, particles are supposed isothermal and only convection is accounted for (no radiative transfer). If the particle is nonreacting (i.e., is an alumina residue), the convective heat term is

$$Q_v = \pi\lambda_g D\,Nu\,N_p(T_g - T_p) \qquad Nu = 2 + 0.6\,Re_p^{1/2}\,Pr^{1/3} \tag{8}$$

with the correlation for the Nusselt number taken from [23].

If the particle burns, we classically have the energy balance $Q_v = \dot\omega L_v$, meaning that all convective heat received is used for feeding evaporation. In that case, this former relation inserted in the

source term of the particle energy equation of Eq. (2) leads to $T_p = \text{const}$, which is expected because of constant temperature during phase change. This constant is taken to the saturation temperature of aluminum T_{sat}.

This modeling, although simple, has been successfully used for instability predictions in actual solid rocket motors [8,24,25].

B. Numerical Method

Compressible Navier–Stokes equations are solved using the CPS in-house code [26]. This code adopts a finite volume technique on unstructured mesh. Conservative variables are calculated at the center of each computational cell whereas convective fluxes are computed at cell edges using an approximate Riemann solver (Roe scheme) for the gas phase and a donor-cell-type scheme for the particle phase. An operator splitting is used for source terms when using explicit time stepping: first, conservative variables $\mathbf{W}^n$ are updated without source terms to an intermediate state $\mathbf{W}^*$ for time step Δt. Then, the differential equation $\mathrm{d}\mathbf{W}/\mathrm{d}t = \mathbf{S}$ is solved from $\mathbf{W}^*$ to final state $\mathbf{W}^{n+1}$.

Presented computations are second order accurate in space (MUSCL approach) and second order accurate in time using explicit two-step Runge–Kutta time stepping. All computations are performed in 2-D axisymmetric formulation. The time step is given by a Courant–Friedrichs–Lewy (CFL) criterion set to CFL = 0.8.

C. Model Motor and Computational Domain

Figure 1 shows the physical model examined herein, a large solid rocket motor with simple cylindrical geometry. The port radius is chosen at $R = 0.5$ m and the grain of length $L = 7$ m ends with a nozzle with a throat of radius $R_t = 0.175$ m located by $x_t = 7.3$ m. Only the upper half is treated due to symmetry around centerline $r = 0$.

The computational grid consists of 42,000 quads with about 500×80 points in the axial and radial directions, respectively, for the cylindrical part. The grid is clustered near the burning surface to resolve the aluminum distributed combustion. A posteriori analysis of computations shows that about 20 grid points lie in the combustion zone. The smallest grid spacing at the propellant surface is about 1 mm. Grid convergence has been checked by running computations on a 100,000 grid points mesh and no significant differences have been noted.

Gas and aluminum particle properties chosen have been compiled in Table 1. Physical data concerning particles are typical of burning aluminum and are taken from [17].

Turbulence is not explicitly modeled in the present computations. This is justified here because the motor is rather short, with $L/R = 14$. Indeed, it is generally accepted [27,28] that the laminar/turbulent transition is observed beyond $x/R = 20$, so that a laminar flow is maintained throughout the whole motor in our case.

D. Boundary Conditions

No-slip conditions are used for wall modeling (head-end and nozzle). Flow symmetry is assumed at the centerline. Propellant burning is modeled by an injection boundary condition with imposed mass rate (normal to the surface) and stagnation temperature for gas and particles. Boundary conditions are summarized in Table 2 and detailed hereafter.

For an actual propellant, aluminum particles are largely altered by an agglomeration process taking place at a burning surface. As a general rule, unagglomerated aluminum particles are small so that they will burn very close to the surface, leading to submicron alumina residue smoke. On the other hand, aluminum agglomerates are far bigger and lead to a distributed combustion which can no longer be assumed to be a surface process (recalling that the combustion time is roughly proportional to D^2).

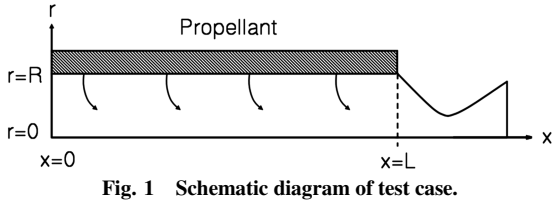

Fig. 1 Schematic diagram of test case.

Table 1 Gas and particle properties used

μ	9.1×10^{-5} kg/m/s
Pr	0.4
γ	1.16
$C_{P,p}$	1177 J/kg/K
$C_{P,g}$	2000 J/kg/K
ρ_p	2000 kg/m^3
Q	9.53×10^6 J/kg
L_v	10.8×10^6 J/kg
T_{sat}	2791 K

According to the experimental results from Duterque [29] on a typical propellant loaded with 18% aluminum, one-third of this aluminum is liable to agglomerate, yielding particles with average diameter about 120 μm. The combustion of those agglomerates then leads to oxide residues of size $D_{\text{res}} = 60$ μm that will no longer burn.

As present two-phase computations are only single class, we chose to focus on that agglomerated fraction of particles because they will involve significant distributed combustion. From the aforementioned Duterque results, we then impose $\kappa_{\text{inj}} = 0.06$. The remaining unagglomerated fraction is supposed to burn on the surface and, from a computational view, is lumped with the gas injection. Therefore, an equivalent injection gas temperature $T_{g,\text{inj}}$ must be calculated, using a simple energy and mass conservation, in such a way that equilibrium flame temperature T_f for the initial propellant considered is recovered in the core flow (with T_f set to 3600 K in the present case). In all forthcoming computations, we systematically check that $T_g \sim T_f$ (within a few Kelvin) in the chamber once particles have completely burned.

Particles are supposed to be injected from the propellant surface while burning (hence $T_{p,\text{inj}} = T_{\text{sat}}$) and in dynamic equilibrium with gas (i.e., $\mathbf{U}_{p,\text{inj}} = \mathbf{U}_{g,\text{inj}}$). All the boundary conditions (as well as D_{res}) are recalled in Table 2.

III. Simulation Results

A. Results on Model Motor

First, single-phase (only gas) computations are performed. Thermodynamic properties and injection boundary conditions (mass rate and injection temperature) are chosen in such a way that both single- and two-phase results are equivalent (in terms of pressure or sound velocity) and can be compared.

The simulation predicts the motor to be completely stable. Of course, this is anticipated because no propellant response is accounted for (constant mass rate assumed) and no vortex shedding is expected due to the simple geometry (no obstacles, no cavities, and $L/R = 14$ is too small for a PVS to develop). Computed head-end pressure is $p = 8.71$ MPa. Slight perturbations are added to the mean flow to get pressure disturbances, the spectral analysis of which allows one to estimate the first axial acoustic mode frequency f_{1L}. We get $f_{1L} \sim 76$ Hz, which is not far from the usual closed-pipe approximation $a/2L = 76.6$ Hz with $a = 1073$ m/s. Two-phase simulations with particles supposed inert (no combustion accounted for) lead to similar stable results.

Table 2 Injection boundary conditions

$m_{g,\text{inj}}$	23 kg/m^2/s
$T_{g,\text{inj}}$	3450 K
$m_{p,\text{inj}}$	1.47 kg/m^2/s
$T_{p,\text{inj}}$	2791 K
D_{inj}	120 μm
D_{res}	60 μm

Surprisingly, the motor experiences an unstable behavior on the first axial acoustic mode when aluminum combustion is taken into accounted. A striking feature is that no vortex sheddings are noticed, meaning that a genuine combustion instability is taking place. Usually, combustion instabilities in solid rocket motors are reported to arise from a solid propellant response (and not from aluminum) and are either on bulk mode (L^* instability) or on high-frequency transverse modes. To the authors' knowledge, this kind of instability has not been simulated in a solid rocket motor configuration so far.

Figure 2 displays the head-end pressure signal and its spectrum. Pressure clearly denotes an unstable behavior with quasi-harmonic character and rms pressure fluctuations calculated to about 19 kPa (0 to peak). Average pressure is about 8.71 MPa, identical to single-phase results as expected. The pressure spectrum confirms that the instability takes place mostly on the first axial mode $1L$ with very few harmonics, as $2L$ or $3L$ modes are hardly visible. The dominant frequency is calculated to be $f = 71.5 + / - 0.5$ Hz. Note that this frequency is the instability frequency, which can slightly differ from the acoustic frequency (obviously not too much for a coupling with acoustics to occur).

Figure 3 shows an instantaneous map of vorticity in the aft part of the motor. Coherent structures, typical of vortex shedding, are missing and only the "zebras," characteristic of the acoustic boundary layer [30], are being observed. As previously told, it is checked that in the core flow (once aluminum combustion is completed), expected values are obtained (particularly gas temperature $T_g = 3600$ K and particle diameter $D = D_{\text{res}} = 60\ \mu$m).

B. Thermoacoustic Nature of Instability

We now demonstrate that this instability is of a thermoacoustic nature and results from a coupling between acoustics and aluminum combustion. The effect of heat release on motor stability can be investigated using the well-known Rayleigh citerion [31], which determines the conditions for driving or suppressing flow oscillations when thermal energy is added (or subtracted) periodically to (or from) the acoustic field. It can be estimated by calculating the Rayleigh parameter $\overline{p'q'}$, which is the time-averaged product between pressure and heat release fluctuations over one period. The exact expression for q' due to burning aluminum particles is obtained by considering two-phase conservation equations and recasting them in terms of a fluctuating pressure equation. Details are given in Appendix and it is found that $q' \approx (\gamma - 1)(C_{P,p}T_{\text{sat}} + Q)\dot{\omega}'$ [Eq. (A3)].

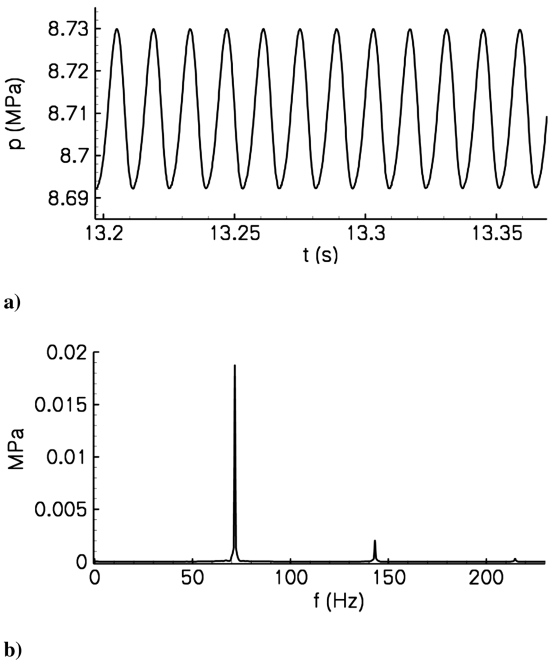

Fig. 2 Head-end pressure: a) history and b) spectrum.

Fig. 3 Instantaneous vorticity contours (aft part).

Figure 4 shows the contours of Rayleigh criterion for the first acoustic mode as well as its axial distribution inside the combustion zone, very close to the surface ($r/R = 0.99$). For the sake of clarity, the radial direction has been stretched by a factor of 10 in Fig. 4a for making the combustion zone more visible. Obviously, it is noted that $\overline{p'q'} = 0$ outside the combustion zone because there is no longer heat release due to combustion. Values of $\overline{p'q'}$ are positive (solid lines) in the first half of the motor indicating a potential to drive unsteady motions, while negative (dashed lines) in the second half. More precisely, the shape of the axial distribution of the Rayleigh parameter inside the combustion zone is close to a sine wave as shown in Fig. 4b. The presence of the no-slip wall at $x = L$ is seen to slightly perturb this distribution. The theoretical developments in Sec. V will explain this sine-wave shape.

Following Rayleigh [31], the global system is liable to be unstable if the following inequality is fulfilled:

$$\int_V \int_T p'q' \mathrm{d}V\mathrm{d}t = \int_V \overline{p'q'}\mathrm{d}V > 0 \tag{9}$$

Integrating $\overline{p'q'}$ on the motor volume leads to an overall positive value: this proves that the motor might possibly experience an instability via thermoacoustic coupling. This is consistent with Fig. 4b where the positive part seems to give a larger contribution than its negative counterpart.

We propose another numerical experience to confirm the thermoacoustic nature of this instability. In the computation, aluminum combustion mass release rate $\dot{\omega}$ is now prescribed to remain at a constant value (taken as its time-averaged value) for each computational cell. Thus, this imposes neither mass release fluctuations ($\dot{\omega}' = 0$) nor heat release fluctuations [$q' = 0$ using Eq. (A3)]. When running the computation, it is observed that the instability damps until a stable regime, although the mean flow remains unmodified. This demonstrates that the instability is driven by aluminum combustion.

Likewise, let us consider the expression for mass rate $\dot{\omega}$ [Eq. (4)] and similarly impose a constant (time-averaged) value to one of the

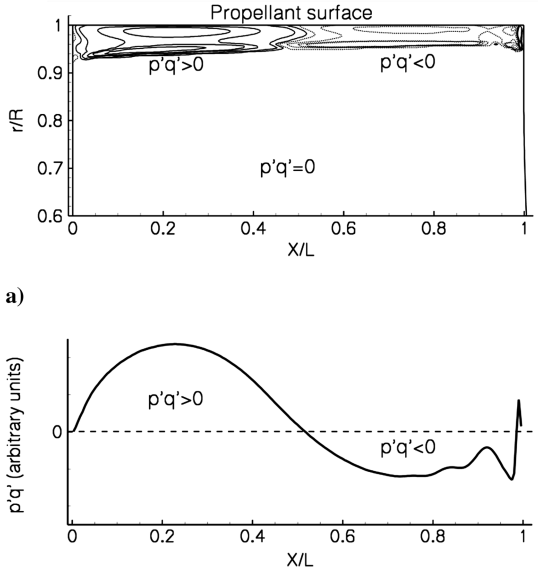

Fig. 4 Rayleigh parameter $\overline{p'q'}$: a) contours in the motor; b) axial distribution at $r/R = 0.99$.

variables, allowing the others to remain untouched. Doing so for the different variables of Eq. (4) leads to the following result: the flow turns stable only in the case where the Reynolds number Re_p is set constant. Imposing no fluctuations to the other variables (for instance B or N_p) does not modify the instability. Figure 5 shows the head-end pressure signal when Re_p fluctuations are canceled (Re_p imposed to a time-averaged value): this clearly demonstrates that the thermo-acoustic coupling is broken here. Additionally, by considering rms fields for all the variables, it is noticed that, in the combustion zone, the relative fluctuations of Re_p are 2 or 3 orders of magnitude larger than the relative fluctuations of N_p, D, or $\ell_n(1+B)$, which confirms that fluctuations of the latter variables have virtually no effects.

This proves that convection is the chief physical process and that aluminum combustion primarily does respond to acoustic velocity, which is not surprising as aluminum flame is diffusion limited. The importance of this direct particle combustion-acoustic velocity interaction was also anticipated by Raun and Beckstead in their Rijke burner model [19]. Although they did not take it into account (assuming combustion in a quiescent atmosphere), they suggested at that time that it could explain why their model underestimated the experimental instability growth rate. Our results show they were indeed right.

On the basis of this consideration, Fig. 6 represents a sketch of the supposed physical phenomena occurring when an aluminum droplet leaves the propellant surface and burns. A flame disturbance is expected to be induced by the acoustic fluctuation u'_g that will sweep the flame envelope and modify the flame area and heat release. Note that this physics is included in the model through Eq. (4) via the simple empirical Ranz–Marshall correction.

IV. Parametric Study

The following parametric study aims at improving the understanding of this kind of instability and also determining the most relevant parameters, especially the ones concerning aluminum combustion.

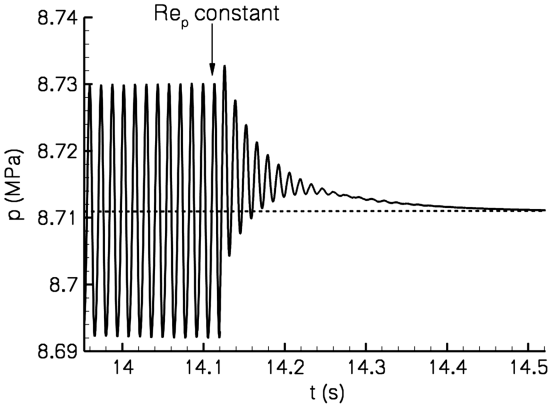

Fig. 5 Pressure signal with no Re_p fluctuations. This proves primary convective control.

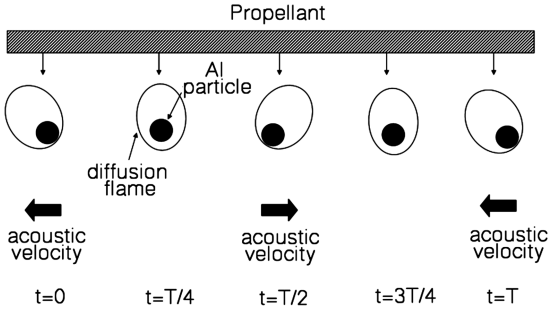

Fig. 6 Sketch of assumed instability mechanism (inspired from [19]).

A. Effect of Aluminum Burn Rate

Aluminum combustion is suspected to play a major role and the effect of the aluminum burn rate is now investigated. Yet, the complexity of aluminum combustion is such that burn rate predictions largely rely on empirical correlations. Moreover, the overall mass release rate predicted could also be lowered by group combustion effects in an actual configuration. Hence, from a practical point of view, it is important to estimate to which extent this instability is liable to be altered by the aluminum burn rate. As a consequence, this parametric study gives information on how crucial the aluminum combustion modeling may be.

Simulations are performed by slightly modifying the expression for burn rate $\dot{\omega}$ in Eq. (4), which is now multiplied by a constant factor in order to change the aluminum burn rate and combustion thickness consequently. All the other parameters are kept at their values.

Figure 7 presents the 0-to-peak head-end pressure level ($\sqrt{2}$ times rms value) as a function of the combustion thickness. This combustion thickness is computed as the distance at which particle diameter D reaches its final value D_{res} within 1%. As this thickness is very slightly varying with axial position, the value is averaged along the motor length.

It can be seen that the instability develops only in a range of combustion thickness (and thus combustion burn rate). When aluminum combustion is too much spatially distributed (thickness beyond 30 mm), the instability dies out. On the opposite, a surface combustion does not involve any coupling with acoustics either. The instability develops on the first acoustic mode $1L$, except when combustion is very close to the surface where a second longitudinal mode $2L$ can be locked on. These computations show that the combustion thickness is a leading-order parameter and that coupling is only possible for a given range of the aluminum combustion rate. Section V details the fact that this is actually due to the acoustic boundary layer, which induces high acoustic velocity zones favorable for a resonant coupling.

It is concluded that aluminum combustion is of major importance, so that the use of our simple D^2 model becomes questionable. For the sake of comparison with experimental data or empirical correlations, Eq. (4) is recast in terms of droplet combustion lifetime t_c by considering mass continuity at the droplet surface [first component of Eq. (2)]. It is then found (see also [23], p. 577 for details), that

$$t_c = \frac{\rho_p Pr D^2}{8\mu\, \ell_n(1+B)} \tag{10}$$

for a quiescent atmosphere and no residue. With our current values, t_c is calculated at 23 ms for $D = 120$ μm. Orlandi [32] reported and compared 10 different empirical correlations for aluminum combustion times and, for a 120 μm droplet, the results ranged between 9 and 44 ms, whereas the widely used Widener–Beckstead

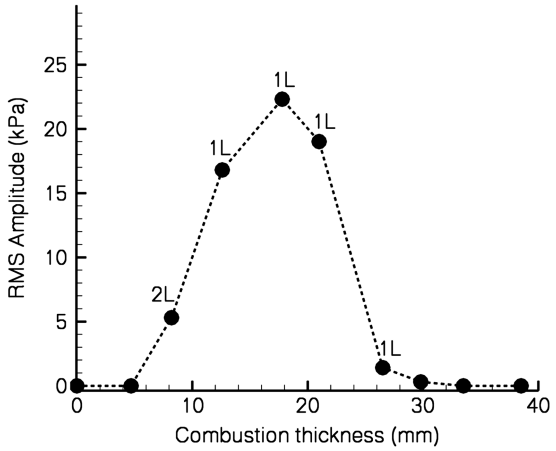

Fig. 7 Thermoacoustic instability level vs aluminum combustion thickness.

correlation [33] gives a value of 28 ms. This means that despite its relative simplicity, the used aluminum combustion model gives results in coherence with current know-how and that present computations are physically meaningful.

B. Effect of Heat Release

Because of thermoacoustic nature, it is expected that the heat of reaction Q for aluminum combustion is of primary importance. Furthermore, its value is not exactly known in the frame of combustion in a propellant like atmosphere as different oxidizers (such as H_2O, CO_2, or HCl) are in competition with different kinetics and diffusivities. Our baseline value $Q_0 = 9.53$ MJ/kg has been estimated based on the JANNAF thermochemical database for the following reaction: $2Al_{(g)} + 1.5O_{2(g)} \rightarrow Al_2O_{3(l)}$. Note that this assumes a complete condensation of alumina.

A parametric study is then performed on the heat of reaction Q. However, if Q is changed, the Spalding number B is altered accordingly [Eq. (5)] and so is the aluminum burn rate [Eq. (4)]. But the previous computations showed that this parameter is of great importance so that the analysis will certainly be biased. Therefore, the value of Q is modified while leaving the Spalding number B unchanged to keep the same burn rate. To do so, the latent heat of vaporization L_v is slightly adjusted to keep B constant. It is expected to induce negligible effects on the underlying physics. Computational results are systematically checked to confirm that the combustion thickness remains unmodified.

Figure 8 presents the 0-to-peak head-end pressure level with respect to the heat of reaction Q (expressed in terms of Q/Q_0 ratio, with baseline $Q_0 = 9.53$ MJ/kg). The striking feature is the S shape with the presence of a threshold value. If Q is lower than approximately $0.7Q_0$, then the instability does not manifest and the motor is absolutely stable. On the contrary, beyond this threshold, the instability seems to be rather independent of the actual value of Q. Again, this means that limited discrepancies on this parameter do not have profound modifications on the physical relevance of the present computations.

The particular case $Q = 0$ corresponds to pure vaporization. In that case, the fact that there is no instability confirms that it is driven more by heat release rather than sole mass release. Vaporization could potentially drive acoustic waves as shown by Dupays and Vuillot [17] but, in that case, its participation, if any, is sufficiently modest to be overwhelmed by acoustic losses.

In the frame of a linear stability approach, this S shape may be reasonably explained if one assumes that the instability growth rate is largely controlled by the value of Q. If this term is large enough to compensate acoustic losses, then the instability can grow. On the contrary, reducing Q induces a small growth rate, lower than the motor damping rate, and stability is promoted.

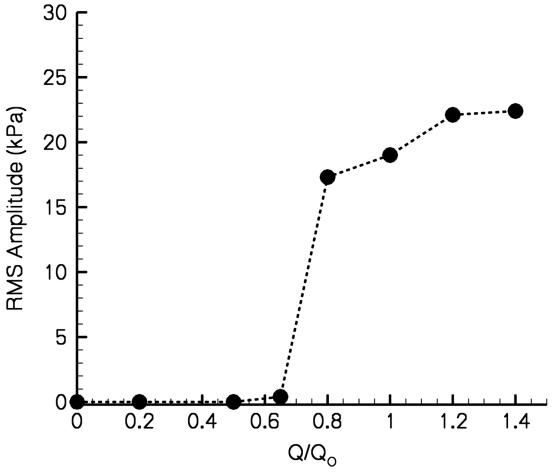

Fig. 8 Thermoacoustic instability level vs aluminum heat of combustion.

Table 3 Computed test cases

No.	κ_{inj}	D_{inj}	D_{res}	Comment
0	0.06	120 μm	60 μm	Baseline
1	0.06	120 μm	1 μm	No residues
2	0.18	30 μm	1 μm	No agglomeration
3	0.12	120 μm	60 μm	Increased κ_{inj}
4	0.06	90 μm	1 μm	Small agglomerates

C. Effect of Particle Diameter

Aluminum particle size is largely altered by a complex, and hardly known, agglomeration process taking place at a burning surface. A detailed study on agglomeration effects would imply parametric study on aluminum particle diameters D_{inj}, alumina residue diameters D_{res}, and injected particle mass fraction κ_{inj} which would be tedious and computationally expensive.

Rather, it is proposed to consider a limited number of different hypotheses on particle diameters and evaluate how strong the impact on the results is. The intended scenarios are compiled in Table 3.

The value of 1 μm for D_{res} roughly corresponds to the size of alumina smoke.

For all these cases, the unagglomerated fraction (lumped with gas injection) and the total energy release, which scales as $(D_{inj}/D_{res})^3$, are different. As already described in Sec. II.D, the gas injection temperature $T_{g.inj}$ is then adjusted, for each computation, in a way that the equilibrium flame temperature $T_f = 3600$ K is recovered in the core flow. This insures that all the computations have identical pressure, sound velocity, or flow parameters. Results are presented in Table 4 with the instability level still expressed by 0-to-peak rms head-end pressure.

It is recalled that computation 0 corresponds to the reference case previously computed.

Case 1 intends to estimate the absence of large alumina residue by only allowing for smoke (1 μm). In that case, the motor is stable which seems to be due to the extra burning time needed to achieve complete droplet combustion. The combustion zone is enlarged accordingly and becomes too thick for a coupling to occur, as already noted. Indeed, considering results from Fig. 7, a combustion thickness of 33 mm was not reported to involve instabilities.

Case 2 allows for no agglomeration (initial aluminum, supposed at 30 μm, ejected and giving only alumina smoke). This time, the droplet lifetime is too short for the combustion to be significantly distributed. In that case again, the motor is stable due to surface combustion (cf. Fig. 7). This represents an a posteriori validation for having only considered aluminum agglomerates in two-phase computations and not the unagglomerated particles supposed to burn at surface and lumped with propellant gas.

Case 3 is similar to reference case 0 but with increased injected particle mass fraction (two-thirds of the total aluminum is now supposed to agglomerate instead of one-third). The combustion zone thickness is not modified. The instability level does not change substantially, going from 19 to 21 kPa. This means that the instability is rather insensitive to the number (or mass fraction) of burning particles. This also relaxes the need of having accurate estimation of agglomeration fraction as a rough estimation should fit.

Case 4 considers smaller particles (90 μm instead of 120 μm) with no residues. This choice leads to the same combustion thickness (22 mm) as the reference case 0. Again, the instability level is not

Table 4 Effect of particle size on instability level

No.	Instability level, kPa	Combustion thickness, mm
0	19	22
1	0	33
2	0	4
3	21	22
4	22	22

profoundly modified which basically means that the size itself of the particles is not so important and that the combustion thickness is the driving parameter.

This parametric study definitely confirms the crucial role of the spatial distribution of the combustion, compared to particle diameter or mass fraction which seems to act much less.

D. Effect of Acoustic Frequency

Acoustic resonance suggests some frequency accordance with acoustic modes. To evaluate the most favorable range of frequencies for the thermoacoustic instability to occur, the acoustic longitudinal mode of the motor has been modified by changing grain length L (recalling $f_{1L} \sim a/2L$). However, it is essential to keep the same burning surface to throat area ratio S_{comb}/S_t to maintain identical chamber pressure and injection gas velocity v_{inj} (v_{inj} is known to largely determine nozzle admittance or acoustic boundary layer, for instance). As a result, when L is changed, the throat radius is altered accordingly.

Figure 9 presents the evolution of the instability level with respect to theoretical first longitudinal acoustic frequency $f_{1L} = a/2L$. The results clearly show that the instability is liable to develop in a narrow range of frequency, typically from 60 to 80 Hz for the current choice of parameters. If the motor acoustic mode does not lie within this range, then the frequency mismatch between acoustics and combustion is too large for the resonance to occur. The question of the frequency of the combustion process will be addressed later on. A last comment on Fig. 9 is that it has not been possible to consider frequencies lower than roughly 60 Hz. In that case, the motor is sufficiently long (in terms of L/R ratio) so that a PVS develops along the grain. This case is not considered in the present study because it involves two powerful instability sources at the same time and the sole effect of thermoacoustic instability can no longer be accurately evaluated. As a matter of fact, the observed drop in the instability level may arise from complex interactions between PVS and aluminum combustion.

V. Theoretical Analysis

A. Linear Stability Theory

The goal of this section is to prove theoretically the existence and some characteristics of the two-phase thermoacoustic instability numerically studied. To do so, we will strongly rely on the pioneering works from Culick [34] who was among the first to assess solid motor stability by theoretical arguments. Such an approach, also known as the acoustic balance theory, is based on linearized fluid mechanics equations assuming small-amplitude pressure fluctuations and low Mach number. Validity domain for this analytical approach has been extended accounting for nonlinearities [35–37] or vortical effects [30,38] and is now widely used in the solid rocket community [39]. Nevertheless, the effects of two-phase flows on stability have only been incorporated for nonreacting particles, giving a well-known

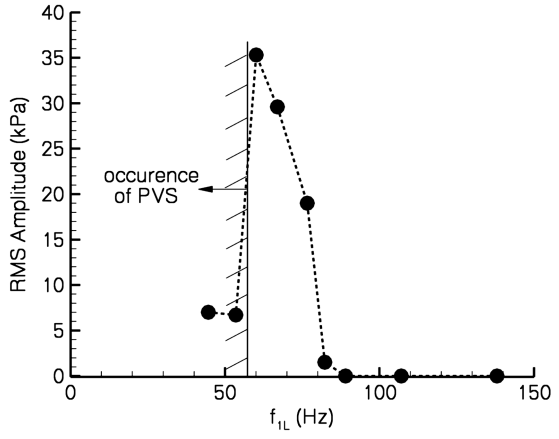

Fig. 9 Thermoacoustic instability level vs acoustic frequency (first mode).

inert particle damping term (let us mention, however, that such inert particles are liable to drive hydrodynamic instabilities in some solid rockets [24,25]). A reliable explicit term for particle combustion contribution may not seem to have been formulated so far and is still lacking in classical linear stability predictions.

The present approach does not claim to devise a complete and complex analysis but at least retain the most important terms to help in shedding light on this combustion instability. From now on, we closely follow the approach from Culick [5,40]. First, an equation on pressure p is obtained [see Eq. (A1)]. Variables are then classically decomposed as sums of mean and fluctuating parts ($p = \bar{p} + p'$, etc.) and equations are written to second order in fluctuations and combined to obtain a nonlinear wave equation $\Box^2 p' = h$ with $\Box^2$ the classical wave operator (d'Alembertian). Then, harmonic modes are sought for, and their growth rates α are considered to either assess or not the linear stability of the motor.

Keeping Culick's formalism, time-space decomposition, for mode n, is such that $p' = \hat{p}e^{i\omega t}$ and $\hat{p} = \bar{p}\eta_n\psi_n$ with η_n the mode amplitude and ψ_n the unperturbed mode shape. Conservation equations also yield for gas velocity vector [40]: $\hat{\mathbf{U}}_g = (ia/\gamma k_n)\eta_n \nabla\psi_n$. The effect of particles [through term q' of Eq. (A2)] appears in one stability integral which is [40]

$$\alpha = \frac{1}{2\bar{p}E_n^2}\int_V \frac{\psi_n \hat{q}^{(r)}}{\eta_n}\mathrm{d}V \quad \text{with} \quad 2E_n^2 = \int_V \psi_n^2 \mathrm{d}V \tag{11}$$

where superscript (r) stands for real part.

For burning particles $q' \approx (\gamma - 1)\dot{\omega}'(C_{P,p}T_{\text{sat}} + Q)$ [Eq. (A3)], so that the growth rate α_{PC} due to particle combustion is

$$\alpha_{\text{PC}} = \frac{(\gamma - 1)(C_{P,p}T_{\text{sat}} + Q)}{2\bar{p}E_n^2}\int_V \frac{\psi_n \hat{\omega}^{(r)}}{\eta_n}\mathrm{d}V \tag{12}$$

Note that this integral is only nonzero in the combustion zone as $\hat{\omega} = 0$ when combustion is completed.

Now, the last development consists of estimating the fluctuating mass release $\hat{\omega}$. Its exact expression may be tedious and difficult to handle. On the other hand, a detailed acoustic balance theory is out of the scope of the present study. Rather, we make use of our computational results to retain the most important effects and neglect the others. The results are detailed in Appendix and it is found that the aluminum combustion fluctuating mass rate is mainly driven by axial gas velocity fluctuations through the relation $\hat{\omega} = H\hat{u}_g$ with H a transfer function given in Appendix [Eq. (A9)]. This means that in the present case, convective effects rule and that this thermoacoustic instability differs from classical thermoacoustic instabilities in burners where we commonly have $\hat{\omega} = H\hat{p}$. This salient distinction arises from the diffusion-limited nature of droplet combustion rather than kinetic control for gas phase combustion.

In the latter expression $\hat{\omega} = H\hat{u}_g$, the fluctuation $\hat{u}_g$ is understood as the unperturbed acoustic axial velocity fluctuation. It is well known that classical "organ pipe" acoustics is generally a good approximation in a solid motor except close to the walls (and thus surface propellant) where an acoustic boundary layer develops [30] and locally modifies velocity fluctuations. This acoustic boundary layer is of great importance here and must be accounted for because particle combustion specifically takes place in the vicinity of the propellant surface. Analytical expressions for acoustic velocity fluctuations in the presence of an injecting surface have been derived by Flandro et al. [30,41] but are a bit complex to handle. As previously remarked, aluminum combustion is limited to the propellant surface region (i.e., $r \sim R$), so that an expression valid there is sufficient. In Appendix , a near-wall approximation of the Flandro theory is proposed by considering a first-order development in the small parameter $\varepsilon = 1 - r/R$. It is found that axial velocity fluctuations accounting for acoustic boundary layer simply read $\hat{u}_g(1 - F)$ [Eq. (B6)] with F a complex number depending mainly on radial distance r. This correction term $1 - F$ can be seen as a modulation of the unperturbed acoustic velocity $\hat{u}_g$ that accounts for rotational effects induced by the presence of an injection surface.

Replacing the final expression for fluctuating mass release rate $\hat{\omega} = H(1-F)\hat{u}_g$ in integral Eq. (12), recalling $\hat{u}_g = (ia/\gamma k_n)\eta_n \nabla\psi_n \mathbf{e}_x$, and taking the real part gives the final expression for particle combustion growth rate:

$$\alpha_{PC} = -\frac{(\gamma-1)a(C_{P,p}T_{sat}+Q)}{2\bar{p}\gamma k_n E_N^2}\int_{V_{comb}} [-H^{(i)} + H^{(r)}F^{(i)} + H^{(i)}F^{(r)}]\,\psi_n \nabla\psi_n \mathbf{e}_x \mathrm{d}V \quad (13)$$

where the volume integral is performed in the combustion zone. Expressions for real and imaginary parts of H and F are, respectively, given in Eqs. (A10) and (B6). The bracketed quantity in Eq. (13) is based only on mean flow properties in the combustion zone and depends primarily on r but also slightly on x due to the mean axial velocity gradient.

As already mentioned, our purpose here is to obtain a first estimation of droplet combustion contribution to linear stability using a simple approach. We are aware that the present analysis is just the first step that can be improved, although forthcoming results are going to show that this approach seems to be a sound basis. Recently, Flandro [42] proposed a rigorous self-consistent theoretical framework that accounts for distributed combustion heat release. Even though his paper focuses on single-phase combustion, the method can be naturally extended to reacting two-phase flows. This could be part of some future work and could offer a more general vision of instabilities with two-phase combustion.

B. Stability Predictions

As stressed in the last section, our goal is not to develop a closed analytical form of Eq. (13) to be included in a classical linear stability program. Rather, we will estimate α_{PC} numerically in order to confirm numerical simulations and thereby help to get insight into the instability.

First of all, the shape of acoustic mode ψ_n is deduced from CFD. Practically, computations are run on one period $T = 1/f$ and spatial repartition of Fourier coefficients, for any variable Φ, is computed according to

$$FT(\Phi) = \frac{1}{T}\int_0^T \Phi(t)\exp(i2\pi t/T)\mathrm{d}t \quad (14)$$

Then, the amplitude and phase of acoustic components are derived from the modulus and argument of $FT(\Phi)$. For the present computations, Fig. 10 shows the centerline distribution ($r = 0$) for the nondimensional real part of pressure fluctuations and imaginary part of axial velocity fluctuations, on the first frequency mode $n = 1$. The classical expected shapes for pressure $\psi = \cos(\pi x/L)$ and for axial velocity u_g [a $\sin(\pi x/L)$ distribution] are well recovered. This confirms that for this cylindrical motor, a pure half-wave solution is an accurate approximation. A slight distortion at $x = L$ is, however, noticed, which is mostly due to convective effects (Mach number no longer negligible) and nozzle admittance (which makes u'_g not exactly zero at $x = L$).

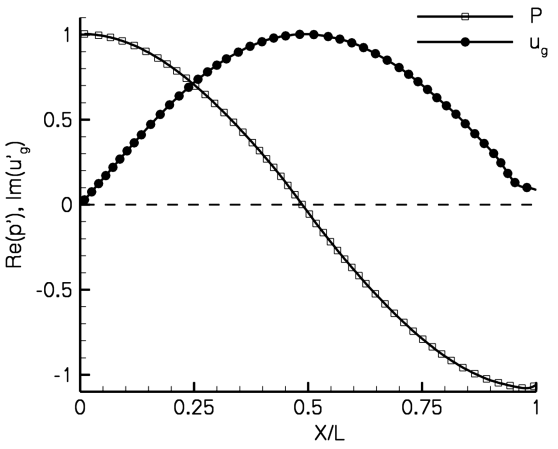

Fig. 10 Computed acoustic mode shape for pressure and axial gas velocity (first mode).

The fact that a coupling exists between pressure and gas velocity [leading to the term $\psi\nabla\psi$ in integral Eq. (13)] can explain the distribution of the Rayleigh parameter that was noticed in Fig. 4. For the demonstration, let us assume that the bracketed term in Eq. (13) depends only on r. Then, as $\psi = \psi(x)$, a variable separation would give

$$\alpha_{PC} \propto \int_0^L \psi\frac{\partial\psi}{\partial x}\mathrm{d}x \propto \int_0^L \cos(\pi x/L)\sin(\pi x/L)\mathrm{d}x = \frac{1}{2}\int_0^L \sin(2\pi x/L)\mathrm{d}x \quad (15)$$

This $\sin(2\pi x/L)$ evolution was the one pointed out for Rayleigh parameter distribution in Fig. 4b with the upper half of the motor ($x < L/2$) giving a positive driving distribution [$\sin(2\pi x/L) > 0$] and negative for the lower half of the motor. In agreement with results from Fig. 4b, the maximum instability region then takes place at one-fourth the length. Let us mention that this is exactly similar to a Rijke tube, for which the heated gauze must be set at $x = L/4$ for maximum thermoacoustic driving.

Note that the integral of Eq. (15) would lead to zero in this case meaning that the destabilizing zones are exactly balanced by the stabilizing ones, inducing a marginal stability ($\alpha_{PC} = 0$). In fact, the bracketed term in Eq. (13) does also depend, albeit weakly, on x through axial mean velocity, so that the variable separation is rigorously incorrect and the integral Eq. (13) is indeed nonzero. Likewise, a motor with complex port shape would have actual acoustic modes differing from the idealized cosine shape, which also leads to a nonzero integral.

Taking advantage of the aforementioned CFD results, the particle combustion growth rate α_{PC} [Eq. (13)] is now evaluated. As it depends on mean flow properties, the time-averaged flowfield is first taken from CFD. Then, α_{PC} is numerically computed directly with the mean flowfield. The integral evaluation yields $\alpha_{PC} = +13.3\ \mathrm{s}^{-1}$ and the positive value of this growth rate proves that the particle combustion contribution is destabilizing in the present case.

To assess motor stability, this value must be compared with other classical acoustic losses, the most important being nozzle admittance α_N and inert alumina residue particles α_{IP} in the core flow. Note that no propellant combustion term is accounted for as it is considered to have a constant mass rate. Other contributions such as attenuation at inert surfaces or viscous damping are neglected. In addition, it is assumed, as stated by Flandro [30,41], that the unsteady boundary-layer pumping mechanism very nearly cancels the Culick flow turning correction, so that the net flow turning can be ignored. For the two conserved terms, classical expressions may be found in the literature [40,41]:

$$\alpha_N = -\frac{v_{inj}}{R}\left[2+\frac{\gamma-1}{2}\right]$$
$$\alpha_{IP} = -\frac{\kappa}{1+\kappa}\frac{\omega}{2}\left[\frac{\omega\tau_d}{1+(\omega\tau_d)^2} + (\gamma-1)\frac{C_{P,p}}{C_{P,g}}\frac{\omega\tau_t}{1+(\omega\tau_t)^2}\right] \quad (16)$$

The evaluation of linear stability for the addressed motor is finally given in Table 5 and proves, in coherence with CFD computations, that the motor is linearly unstable because driving aluminum combustion overcompensates total losses $\alpha_{loss} = \alpha_N + \alpha_{IP} = -11.5\ \mathrm{s}^{-1}$.

Table 5 Linear growth rate estimation

α_N	$-10.8\ \mathrm{s}^{-1}$
α_{IP}	$-0.7\ \mathrm{s}^{-1}$
α_{PC}	$+13.3\ \mathrm{s}^{-1}$
$\Sigma\alpha$	$+1.8\ \mathrm{s}^{-1}$

Actually, the linear growth (or damping) rates, which have been calculated by classical stability theory in Table 5, may also be compared to CFD results. Indeed, some of the computations previously performed appear to turn stable when particle combustion contribution is canceled (such as forcing $Re'_p = 0$ in Sec. III.B or setting $Q = 0$ in Sec. IV.B). In such cases, pressure oscillations then progressively dampen to zero due to acoustic losses, from which a damping rate α_1 may be evaluated. Similarly, using this previous stable solution as a restart, particle combustion is reactivated and pressure oscillations are observed to grow with rate α_2. The results are plotted in Fig. 11. For the two computations just described, head-end pressure signals are first (50–100 Hz) digitally bandpass filtered and the absolute values of pressure peaks are plotted on a log scale versus time. A linear fit gives $\alpha_1 = -12.5\ \mathrm{s}^{-1}$ and $\alpha_2 = +4.4\ \mathrm{s}^{-1}$. This first damping rate $\alpha_1 = -12.5\ \mathrm{s}^{-1}$ corresponds to the only acoustic loss contribution and is found to be pretty close to the expected value from linear stability theory in Table 5: $\alpha_{\mathrm{loss}} = -11.5\ \mathrm{s}^{-1}$. The growth rate $\alpha_2 = +4.4\ \mathrm{s}^{-1}$ includes particle combustion in addition and should then be compared to the overall growth rate $\Sigma\alpha = +1.8\ \mathrm{s}^{-1}$ from Table 5. Finally, it can be deduced from CFD that $\alpha_{\mathrm{PC}} = \alpha_2 - \alpha_1 = +16.9\ \mathrm{s}^{-1}$ in relative coherence with the present estimation from stability integral $\alpha_{\mathrm{PC}} = +13.3\ \mathrm{s}^{-1}$. A slight discrepancy is noticed probably due to the assumptions used in the theoretical developments. However, it means that the formulation of Eq. (13) does account for the main underlying physics and thereby can be used as a first rough estimation of the driving effect of aluminum combustion.

C. Instability Characteristics from Theoretical Analysis

The previous analysis tends to show that the formulated stability integral Eq. (13) is a sound basis for studying the characteristics of this instability. Its existence has been theoretically proven; we now analyze and explain some features of the instability noted in the parametric study. Particularly, it has been remarked that the instability was largely controlled by 1) the aluminum heat of reaction with a threshold critical value (see Fig. 8); 2) the acoustic frequency of the motor (see Fig. 9); and 3) the combustion zone thickness (see Fig. 7).

1. *Effect of Aluminum Heat of Reaction*

The existence of a threshold value on the heat of reaction can be easily explained with regards to the linear stability theory.

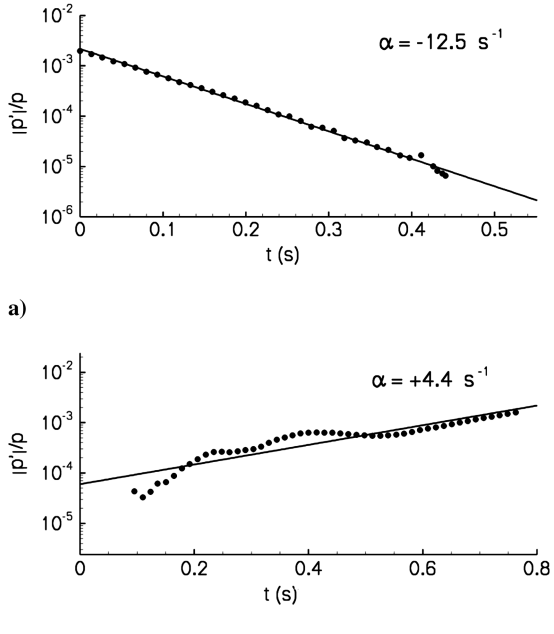

Fig. 11 Growth rates from CFD: a) without particle combustion; b) with particle combustion.

Considering Eq. (13), the value of α_{PC} is found to be proportional to the quantity $C_{P,p}T_{\mathrm{sat}} + Q$. Hence, large values of Q involve high growth rates, possibly large enough to compensate acoustic losses and the instability can grow. On the contrary, lowering Q reduces the growth rate, eventually becoming smaller than the motor damping rate and stability is promoted. This explains the S shape noted in Fig. 8. An additional remark is that even pure vaporization ($Q = 0$) is theoretically liable to drive instability due to the enthalpy injection term $C_{P,p}T_{\mathrm{sat}}$. Practically, this term is much smaller than Q and cannot overcome acoustic losses by itself.

The limit critical value Q_{cr} for the instability to grow is such that $\alpha_{\mathrm{PC}}(Q_{\mathrm{cr}}) + \alpha_{\mathrm{loss}} = 0$. From Eq. (13), we have computed the quantity $\alpha_{\mathrm{PC}} \propto C_{P,p}T_{\mathrm{sat}} + Q_0$ and similarly, the relation $-\alpha_{\mathrm{loss}} \propto C_{P,p}T_{\mathrm{sat}} + Q_{\mathrm{cr}}$ holds with the same proportionality constant if all other parameters are assumed unchanged. This gives the equality $C_{P,p}T_{\mathrm{sat}} + Q_{\mathrm{cr}} = -\alpha_{\mathrm{loss}}/\alpha_{\mathrm{PC}}(C_{P,p}T_{\mathrm{sat}} + Q_0)$ from which the threshold value Q_{cr} is computed to be $Q_{\mathrm{cr}}/Q_0 = 0.81$. This value is pretty close to the one from the CFD computations in Sec. IV.B (see Fig. 8), where the parametric study on Q gives a threshold value by $Q_{\mathrm{cr}}/Q_0 \sim 0.7$.

2. *Effect of Acoustic Frequency*

Results from Fig. 9 suggest that motor acoustic frequency must be roughly in the range 50–80 Hz (at least with the set of parameters chosen) for the instability to lock on acoustics. Lower frequencies might also be favorable but the occurrence of PVS, for the L/R ratio considered then, precludes any conclusions on the role of the sole thermoacoustic contribution.

Frequency dependence of α_{PC} is now investigated. In Sec. V.A, the relation $\hat{\omega} = H(1 - F)\hat{u}_g$ is set with H directly connected to Reynolds number fluctuations Re'_p and F linked with acoustic boundary-layer effects. Actually, both H and F depend on frequency, leading to the overall frequency dependence of the thermoacoustic driving term α_{PC}. Transfer function H depends on frequency because of the inertial response of particles to gas fluctuations: it is a particle-based time scale. On the other hand, F depends on frequency for aerodynamic reasons and is based on injection flow time scale R/v_{inj}.

Taking the real part of $\hat{\omega}$ (recalling $\hat{u}_g$ is pure imaginary) leads to the bracketed term of Eq. (13): $-H^{(i)} + H^{(r)}F^{(i)} + H^{(i)}F^{(r)}$. The first term $-H^{(i)}$ is the contribution from the only particle-gas interactions and, regarding its expression [Eq. (A10)], is maximum at the frequency for which Stokes number $St = 1$. The two other terms arise from some interactions between particles, gas, and acoustic boundary layer and have a more complex frequency dependence, both on Stokes number St and Strouhal number S. Note that without an acoustic boundary layer ($F = 0$), only the term $-H^{(i)}$ is retained in stability integral Eq. (13) but still does give an overall driving effect.

Frequency dependence of α_{PC} is studied by computing integral Eq. (13) while varying the frequency (all other parameters remaining unchanged). To gauge the effects of the acoustic boundary layer, the growth rate α_{PC} without acoustic boundary layer ($F = 0$) is also computed. The results for those two growth rates are plotted in Fig. 12 together with the damping rate $-\alpha_{\mathrm{loss}}$ as the dashed line [note that α_{loss} slightly varies with frequency through the particulate damping term α_{IP}, see Eq. (16)]. This allows one to determine the instability/stability region: the motor is linearly unstable if the gain α_{PC} is above the $-\alpha_{\mathrm{loss}}$ dashed line. Figure 12 gives much information. Let us first consider the α_{PC} with acoustic boundary layer (black circles). It exhibits a wavy shape with several peaks and gives an overall instability in two frequency regions, one in the range (20–80 Hz) and the other, smaller, in the range (120–160 Hz). This result shows that a particle combustion/acoustics resonance is possible because the first acoustic mode lies in this unstable range (20–80 Hz). Likewise, the second longitudinal mode belongs to the (120–160 Hz) region, which possibly explains why a second acoustic mode is sometimes locked on for some flow conditions (see results from Fig. 7). This also clarifies the CFD results from Fig. 9 where the instability was computed to vanish for frequencies above 80 Hz. Besides, simulations performed with $f_{1L} \sim 60$ Hz gave an enhanced

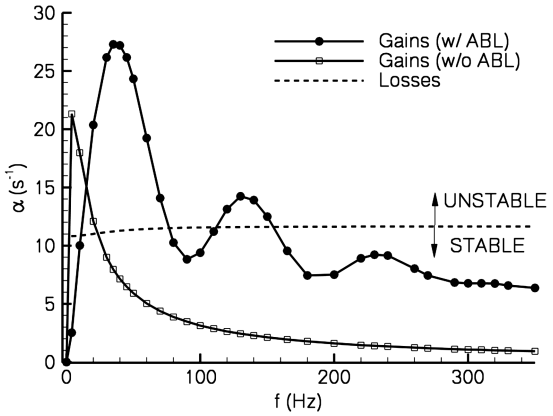

Fig. 12 Growth rates α_{PC} vs frequency [with and without acoustic boundary layer (ABL)].

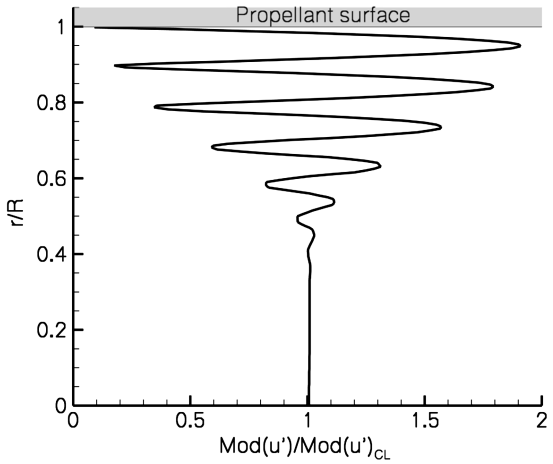

Fig. 13 Transverse profile of axial acoustic velocity module (at $x = L/2$).

instability level, which can be connected with larger α_{PC} as seen in Fig. 12.

A remarkable result is that without acoustic boundary-layer effects (white squares in Fig. 12), the thermoacoustic contribution is still driving but too small to overcome acoustic losses. Ergo, acoustic boundary layer is, at least for the present configuration, a major ingredient in thermoacoustic resonance by promoting an enhanced coupling between combustion and gas velocity fluctuations. Also note that it is the acoustic boundary layer that gives this particular frequency dependence of the thermoacoustic driving term.

It is recalled that the results presented in Fig. 12 are obtained by varying the frequency in the computation of Eq. (13) while keeping the same mean flow. Rigorously, this frequency dependence, and induced stability regions, should then be only valid for our baseline test case.

3. *Effect of Combustion Thickness*

Parametric studies from Secs. IV.A and IV.C lead to the conclusion that the combustion thickness is the main controlling parameter. This can simply be explained by relying on the previous analysis which points out the prominent role of the acoustic boundary layer.

Figure 13 plots the distribution of the module of axial acoustic velocity (at $x = L/2$ and on the first mode f_{1L}) computed by CFD (scaling by centerline value). It clearly outlines a well-known consequence of acoustic boundary layers: close to the surface, the axial velocity module can be increased by a factor up to 2 at the first peak. Driven by this very velocity fluctuation, the thermoacoustic resonance is greatly promoted if the combustion takes place there. From Fig. 13, the acoustic velocity gradient at the propellant surface is computed to be about 300 s^{-1}. This leads to a wall shear stress around 0.03 Pa, which turns out to be as large as the shear from the mean flow.

Although this is a simple analysis (not only amplitude but phase should also be included), this can qualitatively explain the results. If the combustion takes place by the region of maximum u'_g (first peak), then the instability is at its strongest. If the combustion is too close from the surface, then it lies in a region of much smaller u'_g ($u'_g = 0$ at the surface). On the contrary, if the combustion is too much spatially distributed, it will include this previous high u'_g zone but also a less active region with low u'_g (see Fig. 13) and this decreases the overall gain α_{PC} possibly beneath the losses. In addition, the transfer function H is proportional to $\dot{\omega}$, meaning that slow burning particles give smaller a_{PC}.

The frequency pattern noted in Fig. 12 is explained similarly. The frequency of maximum instability in Fig. 12 is obtained when the first u'_g peak is located in the combustion zone. As frequency (and Strouhal number S) increases, velocity peaks induced by the acoustic boundary layer are moving closer to the walls. Hence, a less active region (first "negative" peak) enters the combustion region and lowers the growth rate. As the frequency increases again, the second maximum peak penetrates the combustion zone and favors the instability, which explains the second unstable region (120–160 Hz). And so on with the other peaks, leading to the noted wavy pattern in Fig. 12.

A crude estimation of the most favorable motor acoustic frequency can be performed using this simplified analysis. Considering the expression for F [Eq. (B6)], the maximum of acoustic velocity (in module) is linked with the maximum of the quantity $\|1 - \exp(iS\varepsilon)\| = [2 - 2\cos(S\varepsilon)]^{1/2}$ with ε the nondimensional distance to the surface and S the Strouhal number. This maximum is obtained at the nondimensional distance $\varepsilon_{max} = \pi/S$. Then, for the combustion location to match this highest velocity region, a criterion might be $\varepsilon_{max} \sim \varepsilon_{comb}$. Replacing the expression for the Strouhal number [Eq. (B3)] finally leads to a "rule-of-thumb" estimation for the most favorable frequency $f_{max} \sim v_{inj}/2e_{comb}$ with e_{comb} the combustion thickness. With $v_{inj} \sim 2.6$ m/s and $e_{comb} \sim 22$ mm, this gives $f_{max} \sim 59$ Hz in roughly correct agreement with the parametric study (Fig. 9) or frequency distribution (Fig. 12). This estimation may then be compared with acoustic modes for the first raw estimation of aluminum combustion instability risks.

This analysis stresses the role of the acoustic boundary layer on the driving effect of aluminum distributed combustion. As a final remark, let us outline the fact that turbulence may also possibly play a role. Indeed, for higher L/R ratio motors, where transition is now likely to occur, turbulence is known to dissipate vortical waves and thereby dampens the acoustic boundary layer in the aft part of the motor [43,44]. This could clearly affect the global stability of the motor and has to be checked in the future.

VI. Conclusions

This work details a previously unreported instability in solid rocket motors revealed by numerical simulations. A simple motor, with cylindrical port, is considered and predicted to be stable by single-phase CFD computations. When aluminum combustion is accounted for, the motor experiences a strong instability on the first acoustic mode, despite no vortex shedding being observed. The use of Rayleigh criterion suggests a genuine thermoacoustic instability. Moreover, the instability is suppressed by forcing zero particulate Reynolds fluctuations, which shows that the aluminum combustion primarily responds to acoustic velocity. A scenario is proposed in which the acoustic velocity sweeps the flame envelope of the burning aluminum droplets and then increases the heat release.

A parametric study stressed the importance of some parameters, one of the most important being the size of the aluminum combustion zone. If aluminum combustion is too much spatially distributed or too close to the surface, then the instability does not manifest. A strong effect of aluminum heat of reaction is also demonstrated. Besides, changing the motor length allows setting a range of

favorable acoustic frequencies for the instability to appear. With the current choice of aluminum and flow parameters, the instability ceased for frequency beyond 80 Hz.

To get insight into this instability, the acoustic balance theory has been revisited and an expression for a new stability integral linked with aluminum combustion is proposed. A simplified analytical relation to fit in a standard stability program was not searched for because our primary goal was not to improve this kind of approach. Therefore, the integral is numerically evaluated, based on the mean flow from CFD. It turned out to be a driving term and the motor could finally be calculated to be linearly unstable in agreement with computations. This theoretical background was successfully used to explain quantitatively the results from CFD computations, particularly the salient effects of combustion thickness or aluminum heat of reaction. Likewise, the frequency content of the combustion process is proven to be caused by the acoustic boundary layer which induces alternative regions of high and low acoustic velocities close to the propellant surface. A simplified criterion for expected frequency is given, to be compared with acoustic modes for a first crude estimation of aluminum combustion instability risks.

Further perspectives are linked with the coupling between aluminum combustion, acoustics, and vortex sheddings because they are likely to occur in actual motors. In fact, we believe that the absence of clear experimental evidence for aluminum combustion driving so far might suggest that the thermoacoustic process is possibly overwhelmed by vortex sheddings and that resulting interactions are quite complex. Work is currently in progress.

Appendix A: Equations for Aluminum Combustion Fluctuating Mass and Heat Rates

Conservation equations are recast in a nonconservative form so that the following equation on pressure p is obtained (also found in [40], p. 730):

$$\frac{\partial p}{\partial t} + \gamma p \nabla \cdot \mathbf{U}_g + \mathbf{U}_g \cdot \nabla p = q$$
$$q = (\gamma - 1)\left\{ -Q_v + \mathbf{F}_d \cdot \delta\mathbf{U} + \dot{\omega}\left(C_{P,p} T_p + L_v + Q + \frac{1}{2}\delta\mathbf{U}^2 \right) \right\} \tag{A1}$$

All variables are decomposed as sums of mean and fluctuating parts ($p = \bar{p} + p'$, etc.,. . .) and equations are written to second order in fluctuations. As combustion is considered, we make use of the energy conservation relation $Q_v = \dot{\omega} L_v$ and the fact that droplet temperature is constant during combustion ($T_p = T_{\text{sat}}$ implying $T'_p = 0$). It is found the fluctuating pressure equation:

$$\begin{aligned} &\frac{\partial p'}{\partial t} + \gamma p \nabla \cdot \mathbf{U}'_g + \mathbf{U}_g \cdot \nabla p' + \gamma p' \nabla \cdot \mathbf{U}_g + \mathbf{U}'_g \cdot \nabla p' \\ &\quad + \gamma p' \nabla \cdot \mathbf{U}'_g = q' \\ &q' = (\gamma - 1)\left\{ \mathbf{F}_d \cdot \delta\mathbf{U}' + \mathbf{F}'_d \cdot \delta\mathbf{U} + \dot{\omega}\delta\mathbf{U} \cdot \delta\mathbf{U}' \right. \\ &\quad \left. + \dot{\omega}'\left(C_{P,p} T_{\text{sat}} + Q + \frac{1}{2}\delta\mathbf{U}^2 \right) \right\} \end{aligned} \tag{A2}$$

where the bars denoting time-averaged values have been dropped for the sake of simplicity.

Orders of magnitude for the different terms in the q' expression suggest that only the combustion part should be retained as it overwhelms drag force work and kinetic energy which finally gives

$$q' \approx (\gamma - 1)\dot{\omega}'(C_{P,p} T_{\text{sat}} + Q) \tag{A3}$$

Note that this approximation is mathematically exact in the case of equilibrium between gas and particles because all the neglected terms are (explicitly or not) proportional to relative velocity $\delta\mathbf{U}$.

An expression for $\dot{\omega}'$ is then obtained by perturbing Eq. (4), which yields

$$\frac{\dot{\omega}'}{\dot{\omega}} = \frac{N'_p}{N_p} + \frac{D'}{D} + \frac{(1 + 0.3\, Re_p^{1/2} Pr^{1/3})'}{(1 + 0.3\, Re_p^{1/2} Pr^{1/3})} + \frac{B'}{(1 + B)\,\ell_n(1 + B)} \tag{A4}$$

Recasting this expression rigorously only in terms of acoustic pressure or velocity is tedious and leads to a quite complex formulation beyond the scope of the present study. As we want to focus on the main phenomena, we take advantage of the CFD results obtained. In particular, it is observed that, in the combustion zone, the relative fluctuation of the Ranz–Marshall term is the leading-order one in Eq. (A4) (third term on the right-hand side). Relative fluctuations of N_p, D, or $\ell_n(1 + B)$ are 2 or 3 orders of magnitude lower. This assumption, justified by CFD computations, leads to the simpler expression:

$$\frac{\dot{\omega}'}{\dot{\omega}} \approx \frac{0.15\, Re_p^{1/2} Pr^{1/3}}{1 + 0.3\, Re_p^{1/2} Pr^{1/3}} \frac{Re'_p}{Re_p} \tag{A5}$$

Note that it is coherent with the fact (described in Sec. III.B) that the thermoacoustic coupling may be broken down only by canceling Re_p fluctuations.

Accounting for particulate Reynolds number expression [Eq. (6)] gives

$$\frac{\dot{\omega}'}{\dot{\omega}} \approx \frac{0.15\, Re_p^{1/2} Pr^{1/3}}{1 + 0.3\, Re_p^{1/2} Pr^{1/3}} \frac{\delta u \cdot \delta u'}{\|\delta\mathbf{U}\|^2} \tag{A6}$$

which is obtained under the assumptions that relative fluctuations of density ρ_g and radial velocity v_g are small compared to relative fluctuations of axial velocity u_g. The former assumption is justified by low Mach number M (recalling $\rho'_g/\rho_g = M u'_g/u_g$) and the latter comes from considering axial acoustic modes (hence $v'_g \sim 0$). This has also been checked by CFD computations.

Particle and gas axial velocity fluctuations are such that [17,18]

$$\delta u' = u'_g \left(\frac{iSt - St^2}{1 + St^2} \right) \tag{A7}$$

with the Stokes number St defined by $St = 2\pi f \tau_d$ with τ_d the particle dynamic relaxation time. This relaxation time is obtained through the equation of motion for particles and classically reads $\tau_{d,s} = \rho_p D^2/18\mu$ [17] under Stokes flow assumption. Although such Stokes flow assumption is very widely used, it is only valid in the limit of $Re_p < 1$ which is justified in the core flow but not close to the surface where particles are large and velocity drift is important (values up to $Re_p = 50$ are observed in the present computations). Rather, we use a more general relaxation time expression that includes a Reynolds number correction [45] and reads

$$St = 2\pi f \frac{24}{Re_p C_d} \tau_{d,s} \tag{A8}$$

Combining Eqs. (A6) and (A7) finally leads to the sought expression $\hat{\omega} = H \hat{u}_g$ with H a complex transfer function defined by

$$H = \dot{\omega}\left[\frac{0.15\, Re_p^{1/2} Pr^{1/3}}{1 + 0.3\, Re_p^{1/2} Pr^{1/3}} \right] \frac{\delta u}{\|\delta\mathbf{U}\|^2} \frac{iSt - St^2}{1 + St^2} \tag{A9}$$

and Stokes number St given by Eq. (A8). Note that Eq. (A9) only depends on mean flow properties. Real and imaginary parts are

$$\begin{aligned} H^{(r)} &= -\dot{\omega}\left[\frac{0.15\, Re_p^{1/2} Pr^{1/3}}{1 + 0.3\, Re_p^{1/2} Pr^{1/3}} \right] \frac{\delta u}{\|\delta\mathbf{U}\|^2} \frac{St^2}{1 + St^2} \\ H^{(i)} &= \dot{\omega}\left[\frac{0.15\, Re_p^{1/2} Pr^{1/3}}{1 + 0.3\, Re_p^{1/2} Pr^{1/3}} \right] \frac{\delta u}{\|\delta\mathbf{U}\|^2} \frac{St}{1 + St^2} \end{aligned} \tag{A10}$$

Appendix B: Near-Wall Approximation of Acoustic Boundary Layers

Following Flandro et al. [30], unsteady velocity can be broken up into acoustic (compressible, inviscid, irrotational) and solenoidal (incompressible, viscous, rotational) parts: $\mathbf{U}' = \widehat{\mathbf{U}} + \breve{\mathbf{U}}$.

For a cylindrical motor, the axial acoustic velocity for a longitudinal mode classically reads (see Sec. V.A)

$$\widehat{u} = -\frac{ia}{\gamma}\eta \sin(kx)\exp(i\omega t) \tag{B1}$$

with η the pressure wave amplitude. As for the vortical component, Flandro et al. developed the following expression [30]:

$$\breve{u} = -i\frac{a}{\gamma}\eta\left[B\frac{r}{R}\sin(kx\sin\Theta)\exp\left(\Phi - i\frac{S}{\pi}\ell_n\ \tan\frac{\Theta}{2} + i\omega t\right)\right] \tag{B2}$$

with

$$\Theta = \frac{\pi}{2}\left(\frac{r}{R}\right)^2$$

Exact expressions for complex numbers Φ and B can be found in [30]. They both depend on the Strouhal number S and the viscous parameter ξ defined by

$$S = \frac{\omega R}{v_{\text{inj}}} \qquad \xi = \frac{S^2}{Re_{\text{inj}}} \tag{B3}$$

where v_{inj} and Re_{inj} are the injection velocity and injection Reynolds number, respectively.

Equation (B2) is complex to handle. Moreover, we are only interested in the combustion region, located in the vicinity of the propellant surface. Hence, a simplification in the region $r \sim R$ is sufficient for the present purpose and Eq. (B2) is going to be developed with respect to the small parameter $\varepsilon = 1 - r/R$. In addition, for practical applications, the ratio ξ/S is extremely small because the flow is almost laminar in the viscous sublayer. In the present case, $S \approx 80$ and $\xi \approx 0.05$ leading to $\xi/S \approx 6 \times 10^{-4}$. Under this approximation, parameters Φ and B have simpler expressions and read $\Phi \approx i\pi/S\cos\Theta$ and $B \approx \langle v_g(r)\rangle$ where the mean gas radial velocity can be represented by the Culick mean flow model $\langle v_g(r)\rangle = -R/r\sin\Theta$.

We now develop each term of Eq. (B2) with respect to the small parameter $\varepsilon = 1 - r/R$ and, after a few algebra, this leads to the following second-order approximation:

$$\breve{u} \approx -\widehat{u}\left(1 - \frac{\pi^2\varepsilon^2}{2}\right)\exp\left[i\left(S\varepsilon + \frac{\pi^2}{S}\varepsilon - \frac{S^2}{2}\varepsilon^2\right)\right] + O(\varepsilon^3) \tag{B4}$$

Alternatively, noting that $S \gg \pi^2/S$ and retaining only first-order terms, a much simpler form is obtained:

$$\breve{u} \approx -\widehat{u}\exp(iS\varepsilon) + O(\varepsilon^2) \tag{B5}$$

Second-order and first-order developments [Eqs. (B4) and (B5)] have been validated by comparison with the original formulation Eq. (B2) and they appear to be virtually identical provided that $\varepsilon < 0.15$ for second-order approximation Eq. (B4) and $\varepsilon < 0.08$ for first-order Eq. (B5). For the present computations, the combustion thickness e_{comb} was about 22 mm giving $\varepsilon_{\text{comb}} = e_{\text{comb}}/R \sim 0.04$, which easily fulfills the validity domain even for the first-order approximation.

Thus, the first-order near-wall development of Flandro's formulation yields a simple and easy-to-use approximation for the total unsteady axial velocity:

$$u' = \widehat{u}(1 - F) \quad \text{with} \quad F = \exp(iS\varepsilon) \tag{B6}$$

The complex transfer function F can be seen as a modulation of acoustic velocity due to vortical effects. Theoretical developments on acoustic boundary layer assume a simple gas flow. But the present flow is two phase with combustion, large temperature gradients close to the surface …etc., which could modify results on acoustic boundary layers. As stressed by Flandro [42], additional work is needed to properly evaluate these unsteady boundary effects when two-phase mixing, particle interactions, and vaporization are present. However, comparisons between CFD (e.g., Fig. 13) and theory [Eq. (B2)] show that possible modifications remain limited, meaning that vortical/acoustic interactions are little affected by those side effects such as particles or combustion. This is coherent with the computations from [44] where inert particles are shown not to profoundly modify the acoustic boundary-layer development. This could, however, be a potential cause of discrepancy on growth rate calculations between stability integral and CFD results.

Acknowledgments

This work has been supported by SNPE Matériaux Energétiques and the French space agency Centre National d'Etudes Spatiales (CNES).

References

[1] Scippa, S., Pascal, P., and Zanier, F., "Ariane 5 MPS Chamber Pressure Oscillations Full Scale Firing Results Analysis and Further Studies," AIAA Paper 94-3068, June 1994.

[2] Blomshield, F. S., and Bicker, C. J., "Pressure Oscillations in Shuttle Solid Rocket Motors," AIAA Paper 97-3252, July 1997.

[3] Brown, R. S., Dunlap, R., Young, S. W., and Waugh, R. C., "Vortex Shedding as a Source of Acoustic Energy in Segmented Solid Rockets," *Journal of Spacecraft and Rockets*, Vol. 18, No. 4, 1981, pp. 312–319. doi:10.2514/3.57822

[4] Dotson, K. W., Koshigoe, S., and Pace, K. K., "Vortex Shedding in a Large Solid Rocket Motor Without Inhibitors at the Segment Interfaces," *Journal of Propulsion and Power*, Vol. 13, No. 2, 1997, pp. 197–206. doi:10.2514/2.5170

[5] Culick, F. E. C., "Unsteady Motions in Combustion Chambers for Propulsion Systems," RTO AGARD RTO-AG-AVT-039, 2006.

[6] Shu, P. H., Sforzini, R. H., and Foster, W. A., "Vortex Shedding from Solid Rocket Propellant Inhibitors," AIAA Paper 86-1418, June 1986.

[7] Stubos, A. K., Benocci, C., Pallo, E., Stoubos, G. K., and Olivari, D., "Aerodynamically Generated Acoustic Resonance in a Pipe with Annular Flow Restrictors," *Journal of Fluids and Structures*, Vol. 13, No. 6, 1999, pp. 755–778. doi:10.1006/jfls.1999.0226

[8] Guéry, J. F., Gallier, S., Dellapieta, P., and Godfroy, F., "Numerical Simulations of Thrust Oscillations of Segmented AP/AL Solid Rocket Motors," IAF 01-S.2.05., Oct. 2001.

[9] Lupoglazoff, N., and Vuillot, F., "Parietal Vortex Shedding as a Cause of Instability for Long Solid Propellant Motors. Numerical Simulations and Comparisons with Firing Tests," AIAA Paper 96-0761, Jan. 1996.

[10] Avalon, G., Casalis, G., and Griffond, J., "Flow Instabilities and Acoustic Resonance of Channels with Wall Injection," AIAA Paper 98-3220, July 1998.

[11] Vuillot, F., Traineau, J. C., Prevost, M., and Lupoglazoff, N., "Experimental Validation of Stability Assessment Methods for Segmented Solid Propellant Motors," AIAA Paper 93-1883, Jan. 1993.

[12] Ugurtas, B., Avalon, G., Lupoglazoff, N., and Vuillot, F., "Numerical Computations of Hydrodynamic Instabilities Inside Channels with Wall Injection," AIAA Paper 99-2505, June 1999.

[13] Casalis, G., Avalon, G., and Pineau, J. P., "Spatial Instability of Planar Channel Flow with Fluid Injection Through Porous Walls," *Physics of Fluids*, Vol. 10, No. 10, 1998, pp. 2558–2568. doi:10.1063/1.869770

[14] Chedevergne, F., Casalis, G., and Féraille, T., "Biglobal Linear Stability of the Flow Induced by Wall Injection," *Physics of Fluids*, Vol. 18, No. 1, 2006, pp. 014103-1–014103-14.

[15] Kuentzmann, P., "Combustion Instabilities," AGARD LS 180, Paper 7, 1991.

[16] Culick, F. E. C., "Combustion Instabilities in Liquid-Fueled Propulsion Systems: An Overview," AGARD CP450, Paper 1, 1989.

[17] Dupays, J., and Vuillot, F., "Propagation of an Acoustic Wave in a Two-Phase Reactive Medium," AIAA Paper 98-3696, 1998.

[18] Dupays, J., and Vuillot, F., "Propagation of Acoustic Waves in a Two-Phase Vaporizing Mixture," *Journal of Propulsion and Power*, Vol. 18, No. 1, 2002, pp. 222–224. doi:10.2514/2.5924

[19] Raun, R. L., and Beckstead, M. W., "A Numerical Model for Temperature Gradient and Particle Effects on Rijke Burner Oscillations," *Combustion and Flame*, Vol. 94, 1993, pp. 1–24. doi:10.1016/0010-2180(93)90015-U

[20] Brooks, K. P., and Beckstead, M. W., "Dynamics of Aluminum Combustion," *Journal of Propulsion and Power*, Vol. 11, No. 4, 1995, pp. 769–780. doi:10.2514/3.23902

[21] Ranz, W. E., and Marshall, W. R., "Evaporation from Drops," *Chemical Engineering Progress*, Vol. 48, No. 3, 1952, pp. 141–146.

[22] Clift, R., Grace, J. R., and Weber, M. E., *Bubbles, Drops, and Particles*, Academic Press, New York, 1978.

[23] Kuo, K. K., *Principles of Combustion*, 2nd ed., Wiley, New York, 2005, p. 572.

[24] Ballereau, S., Godfroy, F., and Guery, J. F., "Assessment on Analysis and Prediction Method Applied on Thrust Oscillation of Ariane 5 Solid Rocket Boosters," AIAA Paper 2003-4675, July 2003.

[25] Ballereau, S., Godfroy, F., Orlandi, O., and Ballion, D., "Numerical Simulations and Searching Methods of Thrust Oscillations for Solid Rocket Motors," AIAA Paper 2006-4425, July 2006.

[26] Durand, P., Vieille, B., Lambaré, H., Vuillermoz, P., Boure, G., Steinfeld, P., Godfroy, F., and Guéry, J. F., "CPS: A Three-Dimensional CFD Code Dedicated to Space Propulsive Flows," AIAA Paper 2000-3864, June 2000.

[27] Apte, S., and Yang, V., "Unsteady Flow Evolution in a Porous Chamber with Surface Mass Injection, 1: Free Oscillation," *AIAA Journal*, Vol. 39, 2001, pp. 1577–1586. doi:10.2514/2.1483

[28] Apte, S., and Yang, V., "An LES Study of Transition and Flow Instability in a Porous-Walled Chamber with Mass Injection," *Journal of Fluid Mechanics*, Vol. 477, Feb. 2003, pp. 215–225.

[29] Duterque, J., "Experimental Studies of Aluminum Agglomeration in Solid Rocket Motors," *4th International Symposium on Special Topics in Chemical Propulsion (4-ISICP)*, edited by K. K. Kuo, Begell House, Inc., New York, 1996.

[30] Flandro, G., Cai, W. D., and Yang, V., "Turbulent Transport in Rocket Motor Unsteady Flowfield," *Solid Propellant Chemistry, Combustion and Motor Interior Ballistics*, AIAA Progress in Astronautics and Aeronautics, edited by V. Yang, T. B. Brill, and W. Ren, Vol. 185, AIAA, Reston, VA, 2000, pp. 837–857.

[31] Rayleigh, J. W. S., "The Explanation of Certain Acoustical Phenomena," *Nature (London)*, Vol. 18, No. 455, July 1878, pp. 319–321.

[32] Orlandi, O., "Modélisation et Simulation Numérique de la Combustion d'une Goutte Isolée d'Aluminium," Ph.D. Dissertation, University of Orléans, 2002 (in French).

[33] Widener, J. F., and Beckstead, M. W., "Aluminum Combustion Modeling in Solid Propellant Combustion," AIAA Paper 98-3824, 1998.

[34] Culick, F. E. C., "Stability of High-Frequency Pressure Oscillations in Rocket Combustion Chambers," *AIAA Journal*, Vol. 1, No. 5, May 1963, pp. 1097–1104. doi:10.2514/3.1730

[35] Culick, F. E. C., "Nonlinear Behavior of Acoustic Waves in Combustion Chambers," *Astronautica Acta*, Vol. 3, 1976, pp. 715–734. doi:10.1016/0094-5765(76)90107-7

[36] Yang, V., Yang, V., Kim, S. I., and Culick, F. E. C., "Triggering of Longitudinal Pressure Oscillations in Combustion Chambers: 1: Nonlinear Gasdynamics," *Combustion Science and Technology*, Vol. 72, 1990, pp. 183–214. doi:10.1080/00102209008951647

[37] Wicker, J. M., Greene, W. D., Kim, S. I., and Yang, V., "Triggering of Longitudinal Combustion Instabilities in Rocket Motors: Nonlinear Combustion Response," *Journal of Propulsion and Power*, Vol. 12, 1996, pp. 1148–1158. doi:10.2514/3.24155

[38] Flandro, G. A., "Vortex Driving Mechanism in Oscillatory Rocket Flows," *Journal of Propulsion and Power*, Vol. 2, No. 3, 1986, pp. 206–214. doi:10.2514/3.22871

[39] French, J. C., and Flandro, G. A., "Linked Solid Rocket Motor Combustion Stability and Internal Ballistics Analysis," AIAA Paper 2005-3998, July 2005.

[40] Culick, F. E. C., "Prediction of the Stability of Unsteady Motions in Solid-Propellant Rocket Motors," *Nonsteady Burning and Combustion Stability of Solid Propellants*, AIAA Progress in Astronautics and Aeronautics, edited by L. De Luca, E. W. Price, and M. Summerfield, Vol. 143, AIAA, Washington, D.C., 1992, pp. 719–776.

[41] Flandro, G. A., "Effects of Vorticity on Rocket Combustion Stability," *Journal of Propulsion and Power*, Vol. 11, No. 4, 1995, pp. 607–625. doi:10.2514/3.23887

[42] Flandro, G. A., "On the Oscillatory Behavior of Liquid Propellant Rockets," *7th International Symposium on Special Topics in Chemical Propulsion (7-ISICP)*, edited by K. K. Kuo, Begell House, Inc., New York, Sept. 2007.

[43] Apte, S., and Yang, V., "Unsteady Flow Evolution in a Porous Chamber with Surface Mass Injection, 2: Acoustic Excitation," *AIAA Journal*, Vol. 40, 2002, pp. 244–253. doi:10.2514/2.1666

[44] Cai, W. D., Ma, F. H., and Yang, V., "Two-Phase Vorticoacoustic Flow Interactions in Solid-Propellant Rocket Motors," *Journal of Propulsion and Power*, Vol. 19, No. 3, 2003, pp. 385–396. doi:10.2514/2.6142

[45] Dupays, J., "Contribution à l'étude du rôle de la Phase Condensée dans la Stabilité d'un Propulseur à Propergol Solide," Ph.D. Dissertation, Institut National Polytechnique, Toulouse, 1996 (in French).

S. Son
Associate Editor